Dynamic simulation of a Fresnel solar power plant prototype with thermocline thermal energy storage

Sylvain Rodat, Roland Bavière, Arnaud Bruch, Adrien Camus

Dynamic simulation of a Fresnel solar power plant prototype with thermocline thermal energy storage

Sylvain RODAT, Roland BAVIERE, Arnaud BRUCH, Adrien CAMUS

Univ Grenoble Alpes, CEA, LITEN, F-38000 Grenoble, France

Corresponding author: sylvain.rodat@cea.fr

Abstract:

Concentrated solar energy associated with thermal storage is gaining consideration among renewable energy sources since it provides efficient and low-cost solutions along with dispatchability. However, solar energy is intrinsically variable. In this context, a multi-domain numerical simulator can be a valuable aid to tackle the operation and control problems. In the present paper, we build a dynamic model of a concentrated solar power plant prototype using oil as the heat carrier fluid and combining a Fresnel solar field, an Organic Rankine Cycle and a dual media thermocline for thermal energy storage. The simulator takes the form of a large-scale Modelica model including both the physical and the control problems. The model is described component by component and the numerical results are compared to experimental data. Critical operational cases are studied to highlight both the model's capabilities and limitations: startup procedure, storage management and outlet temperature control.

Keywords: concentrated solar energy, dynamic simulation, thermocline thermal storage, control.

1 Introduction

Solar energy can respond to humankind electricity needs. PV (PhotoVoltaic) capacities are rapidly growing with more than 200 GW_{peak} currently installed. However, PV plants are not competitive with CSP (Concentrated Solar Power) plants when energy storage is considered (Stark et al, 2015). Storage is the key component in order to use solar energy as base load. Thermal storage is now unavoidable for future CSP projects. Hybridization could be another option but at the price of a reduced solar share (Soares et al. 2017). The current leading technology is the two-tank thermal storage system. However, reduced costs could be obtained with thermocline thermal storage since this technology relies on a unique tank.

When thermal storage is integrated in a CSP power plant, various options arise for the operator since thermal power can be charged, discharged or directly used in the power cycle. In order to guarantee a baseload capacity with a variable resource, dynamic simulations are required for the sake of optimizing the control of the plant. Many works (Manzolini et al, 2011a, 2011b, Morin et al, 2009) and tools (SAM, Greenius) have been released for steady state simulation of solar power plants to estimate the annual electricity production, generally on an hourly basis. Current researches are focusing on dynamic simulations of solar power plants (Reddy et al., 2013). Among them, works have been dedicated to dynamic simulation for the control of direct steam generation solar power plants (Eck et al, 2007; Birnbaum et al. 2011; Valenzuela et al. 2005). A recent review has been proposed for direct steam generation power plant control (Aurousseau et al., 2016). The present study focuses on monophasic concentrated solar power plants. Recent works have also been published on this topic. Al-Maliki et al.

(2016a, 2016b) propose a simulation of an existing 50 MW parabolic trough solar thermal power plant (ANDASOL II) which includes a two tank thermal storage. The steam cycle is especially detailed. The validation of the model is based on 10 min time-step data that do not give any insight into high frequency dynamic phenomena such as cloud passage. Also, as the measured values come from an operating plant, no specific runs can be carried out for dynamic characterization of the system. The APROS (Advanced Process Simulation Software) is used. Garcia et al (2011) also proposed a simulation of the ANDASOL plant using Wolfram's Mathematica 7. Dymola has also been used for dynamic simulations (Rodat et al. 2014) of monophasic and diphasic solar Fresnel power plants excluding storage. Previously, the automatic control of the 30 MWe SEGS VI parabolic trough plant has been studied (Stuetzle et al., 2004). It operates with oil as heat transfer fluid with no storage capacity. The Archimede solar power plant was also simulated by Manenti et al (2013). It includes a parabolic trough plant using molten salt and a two-tank thermal storage. Two-tank thermal storage positioned in series with the solar field was also addressed by Powell et al (2012). Biencinto et al (2014) proposed a dynamic model to compare two-tank and thermocline thermal storages. These authors point out the need for a smart control of the thermal gradient in the thermocline.

Our topic is the dynamic simulation of a Fresnel power plant prototype including an Organic Rankine Cycle and a dual-media thermocline thermal energy storage. Oil is used both as heat transfer fluid and as storage medium. Even though thermocline thermal storage has already been deeply discussed (Bruch et al., 2014; Pacheco et al 2002; Esence et al. 2017) its coupling with a solar field is of main importance (Ju et al. 2016, Cocco et al. 2015). There is a strong interaction between the thermocline thermal storage and the solar field operation, especially when considering end of charge. Dynamic simulations are particularly required when considering transition cases, for example cloud passage. The control of the maximum fluid temperature requires improved tracking and flowrate regulation algorithms.

The structure of the remaining part of the paper is the following. In chapter 2, the plant and its model are described in details. This includes the receiver and the thermocline storage tank. A simplified model of the Organic Rankine Cycle is considered in the form of a heat sink.

In chapter 3, numerical results are compared to experimental data. This comparison work is performed for the receiver and the heat storage module. The optical and thermal models are adjusted to fit the data from the prototype. An inlet temperature wave transient is used to validate the inertia of the solar field. Dedicated tests on the storage are used to assess the accuracy of the model concerning the axial temperature field in the tank.

In chapter 4, basic control loops are implemented to simulate the whole solar plant. Various transient cases are studied and some technical challenges for solar plant operation are detailed. Chapter 5 synthesizes the present studies and discusses the main findings of the paper.

2 Description and modelling of the solar prototype

2.1 Description of the solar prototype

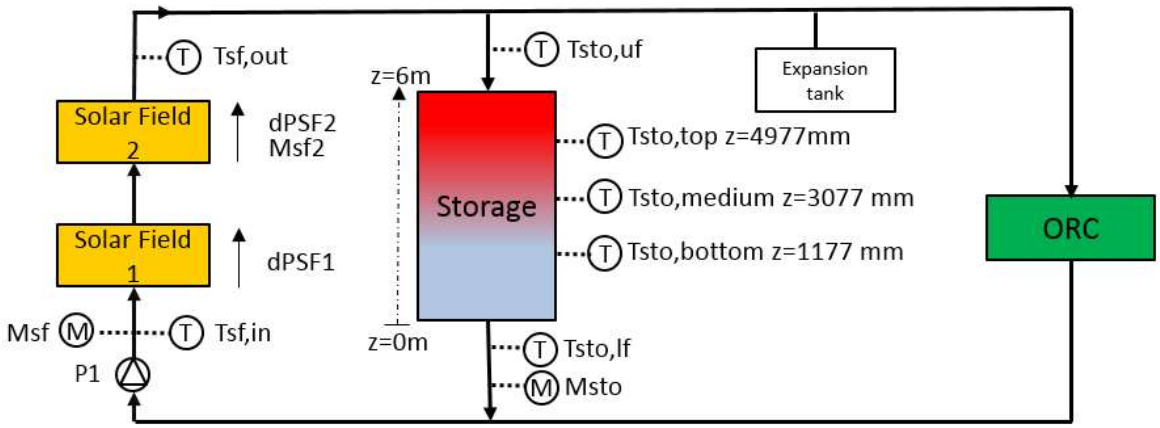

Figure 1 : Scheme of the solar Fresnel prototype (storage in charging mode)

The solar field is based on the Fresnel technology (Rodat et al., 2015). A schematic view is presented in Figure *1*. It consists of a 1000 m² north-south oriented solar field divided into two sections; each of them is composed of ten rows of mirrors 50 m in length. The receiver is a trapezoidal cavity with a multitubular absorber (7 pipes, internal diameter 0.022 m). Thermal oil (Therminol66) is used as heat transfer fluid whereas the working fluid of the 50 kWe Organic Rankine Cycle (ORC) is R245fa. The piping is equipped with temperature sensors (high precision calibrated platinum resistance temperature detectors-uncertainty of +/-0.2 °C), pressure sensors (uncertainty of +/-6 mbar) and Coriolis-type flowmeters (precision of +/-0.1 % of the measure). The input and output temperatures of each solar field are monitored. The maximum absolute operating pressure is 5.5 bar. A 30 m^3 dual media thermocline thermal storage is directly connected to the solar field. The maximum operating temperature of the plant is 300°C. A Kipp&Zonen CHP1 Pyrheliometer for on-site DNI measurement in the spectral range 200 to 4000 nm is also available (expected daily uncertainty of 1 %). The acquisition time step is 2 s which is particularly useful for transient analysis that are in the scope of our study.

The storage tank has been obtained by scaling up a previous prototype described in (Bruch et al. 2014). It is a cylindrical stainless steel tank, 2.5 m in diameter and 6 m in height, surrounded by a dome top and a dished bottom (total 35 m^3). A 300 mm insulation is added to reduce heat losses. The tank is filled with a mixture of silica rocks leading to a bed void fraction of 0.27. The tank is instrumented with inlet/outlet high precision calibrated platinum resistance temperature detectors and embedded K-thermocouples (uncertainty of +/-2.2 °C) on three levels to follow the evolution of the thermal front: 1177 mm, 3077 mm, 4977 mm (0.2, 0.51 and 0.83 in relative height respectively). 5 thermocouples are placed on each level at different locations in order to be able to assess the radial homogeneity of the temperature field. Inlet and outlet temperatures of the tank are also monitored.

2.2 Description of the model

Our numerical simulator is mainly composed of detailed models of the solar field and thermocline storage described in paragraphs 2.2.2 to 2.2.4, along with a simplified model of the ORC considering an ideal heat sink whose output temperature is fixed whatever the inlet temperature. The piping system and the heat exchangers linking these components together are also represented. Finally, the plant control is modelled and this aspect of our work will be described in paragraph 4.

2.2.1 Simulation environment, programming and numerical methods

The numerical simulator is programmed using the Modelica modelling language (Olsson et al., 2014) and executed on the pre- and post-processing simulation platform DYMOLA (Dymola 2017). Modelica allows programming any problem consisting of a set of ordinary differential equations (ODE) or differential-algebraic equations. However, many conservation laws for instance in the fluid mechanics or heat and mass transfer domains are expressed in the form of partial differential equations (PDE). In the present work, we use the finite volume method to discretize these equations. This approach transforms a PDE into a system of ODEs natively tractable by a Modelica simulation engine. Owing to its acausal and object-oriented nature, the Modelica language favors model reusability. In practical terms, our numerical simulator is essentially built by gathering fluidic components already available from the *DistrictHeating* Modelica library (Giraud et al., 2015). The coupling between the different components are performed through the Modelica "connection equation" concept and is therefore seamless to the modeler. Finally, Modelica supports mixtures of continuous and discrete time systems and the language comprises operators suitable for expressing control problems. Relying on this last feature we decided to include the control and the physical problems in a single large-scale Modelica model.

2.2.2 Optical and thermal models of the solar receiver

Optical and thermal models have already been detailed in Rodat et al., 2016 so only their general principles are recalled here.

The receiver is composed of an insulated cavity closed by a window at the bottom and cooled by 7 pipes (see *Figure 2*). The window limits heat losses to the atmosphere while being transparent to most of incoming solar radiations. The top of the cavity is opaque and insulated in order to limit thermal losses.

The optical model consists of an optical efficiency matrix that determinates the heat flux reaching the receiver window for all possible sun positions. The angle step size is 10 °. This matrix is calculated with Zemax ray tracing model (Radiant Zemax, V12). This commercial code was previously used and validated for optical qualification of solar collector (Vidal et al., 2017). The model includes the real 3D (three-dimensional) geometry of the solar field (receiver height, mirror width and shape, reflectivity of the mirror as a function of the incident angle, spacings between mirrors, tracking errors, longitudinal losses) and assumes a global optical error of +/-0.2° (including shape and tracking errors). It is computed for a DNI of 1000 W/m². The optical model also includes the reflectivity of the receiver window since this optical property highly depends on the incidence angle. The limitation of the generated optical matrix is that it gives a mean flux on the receiver (no flux distribution) with a relative coarse discretization (10° angle step). Also it cannot account for soiling of mirrors and glasses and thus a corrective coefficient is applied in order to overcome this limitation (see 3.1).

The model of the receiver is discretized in the axial direction. In the cross-sectional plane, the model is composed of an equivalent pipe of weight 7, a bottom semi-transparent window and a top insulation layer. The thermal and radiative behavior of the window, the tube and the top insulation is represented using 8 temperature nodes (Temperature T1 : outer side of the window; T2 : inner side of the window ; T3 : outer wall of the inferior part of the tube ; T4 inner wall of the inferior part of the tube ; T5 : inner wall of the superior part of the tube ; T6 outer wall of the superior part of the tube T7 : inner side of the insulation ; T8 : outer side of the insulation). The model is depicted in (Figure *2*). It is worth mentioning that the equivalent tube is represented using a single mean temperature for both the superior and inferior surfaces. However the incident solar radiation is supposed to impinge solely the

inferior part of the tube.

The thermal behavior of each solid surface is modelled using two thermal control volumes. The discretization is depicted in Figure 3 for the case of the semi-transparent bottom window. As an example, the heat balance equation considered for temperature node 1 is written below:

$$I_1 \cdot \frac{\partial T_1}{\partial t} = \dot{Q}^{ext \to 1} - \dot{Q}_{cond}^{1 \to 2} + \frac{1}{2} \cdot \phi_1^a + \frac{1}{2} \cdot \phi_2^a - \phi_1^e$$

It includes thermal inertia along with heat exchange by convection, conduction and radiation.

In plane geometry, the conduction term is defined as:

$$\dot{Q}_{cond}^{1 \to 2} = \lambda \cdot \frac{T_1 - T_2}{e}$$

There is a net radiative balance between temperature nodes 2-3 and 6-7. For opaque surfaces, it is computed as the heat transfer between gray, planar, surfaces assuming Kirchoff's law and view factor=1. For semi-transparent surfaces (window), transmission is also considered.

Radiative flux is discretized according to the wavelength l in two bands: IR and visible spectrum with no angular discretization:

$$\phi = \sum e_l \cdot dl$$

Resulting equations for each temperature node are described in details in Rodat et al., 2016.

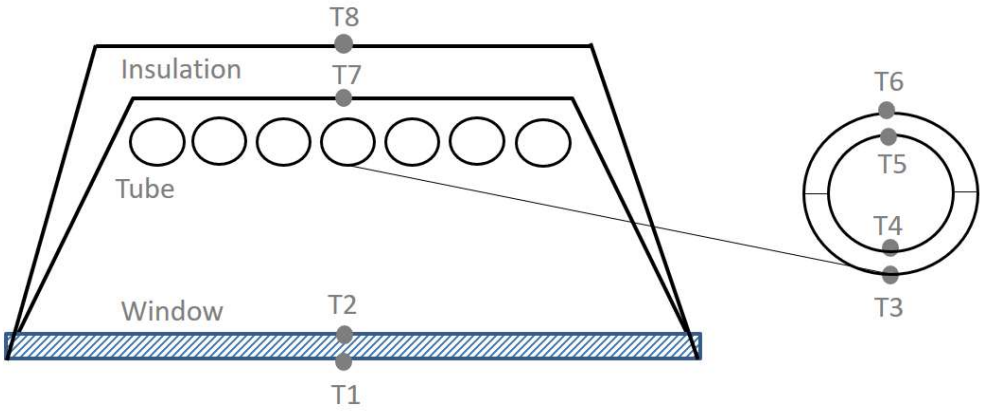

Figure 2 : Cross-sectional view of the solar receiver with temperature nodes (and zoom on a tube section)

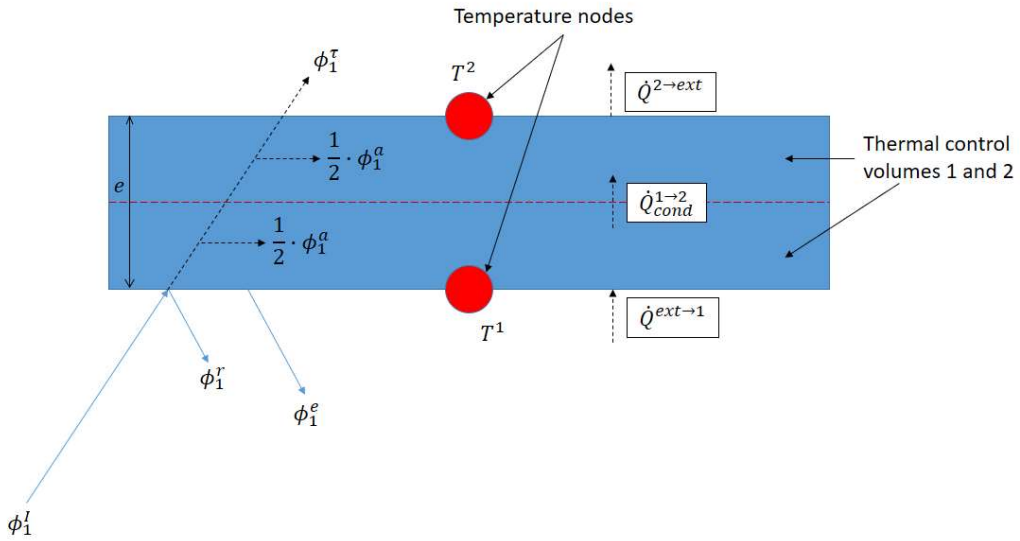

Figure 3 : Heat fluxes and spatial discretization used to model the semi-transparent bottom window of the receiver.

2.2.3 Piping model (receiver pipes and piping)

The pipe model is composed of a series of axially distributed, non-overlapping control volumes. A simplified static momentum conservation equation is written between each control volumes. In this equation, the advection (i.e. spatial acceleration) term is neglected. For each control volume, dynamic mass and energy conservation equations are written in a very usual form, so these are not recalled here. A synthesis of the physical phenomena accounted for is listed below:

-Radial heat conduction through pipe walls

-Tube side heat transfer coefficient

-External thermal losses for all pipes

-External radiative exchanges for the receiver pipes (evaluated through the thermal model, 2.2.2)

-Heat accumulation in the fluid (i.e. convection)

-Heat accumulation in the tube walls

-Regular head losses

Special efforts were dedicated to the definition of correlations for tube side heat transfer coefficient and pressure losses that can be used either for laminar or turbulent flow. Indeed, according to the thermal oil datasheet, its viscosity is high at low temperature and laminar flow is encountered for the startup of the plant. Thus, a good approximation of the convective heat transfer coefficient is required so as to be able to calculate the fluid and wall temperatures during this startup period. Consequently the following expressions where selected and a smoothing equation is proposed in the transitional flow regime:

Tube side heat transfer coefficient:

- For Re <= 1800 $Nu_{lam} = 4{,}36$ (Carvill, 1993)
- For Re >= 3800 $Nu_{turb} = 0{,}012 \times (Re^{0{,}87} - 280) \times Pr^{0.4} \times (1 + (D/L)^{2/3})$
  Simplified expression of the Petukhov-Gnielinski correlation valid for 1.5<Pr<500, 2300<Re<10^6 (Gnielinski, 1976)
- For 1800<Re < 3800 $Nu_{trans} = \frac{Nu_{lam} + Nu_{turb}}{2} + \frac{Re\ -2800}{1000} \times \left(\left(\frac{Re\ -2800}{1000}\right)^2 - 3\right) \times \frac{Nu_{lam} - Nu_{turb}}{4}$

The fluid properties are calculated at the film temperature.

Pressure loss:

Similarly, friction factors are computed over the three flow types with the following equations:

- For Re <= 600 $f_{lam} = \frac{64}{Re}$ (Carvill, 1993)
- For Re >= 1400 $f_{turb} = 0.25 \log(\frac{13}{Re} + \frac{\varepsilon}{3.7D})^{-2}$ (Zigrand and Sylvester, 1965)
- For 600 < Re < 1400 $f_{trans} = \frac{f_{lam} + f_{turb}}{2} + \frac{Re\ -10}{400} \times \left(\left(\frac{Re\ -10}{400}\right)^2 - 3\right) \times \frac{f_{lam} - f_{turb}}{4}$

The transitional flow is considered for Re<1400 in order to have a smoother curve and to limit numerical convergence issues. As a consequence, pressure losses may be slightly overestimated by the model in the transitional flow regime.

2.2.4 Model of the thermocline thermal storage

A 1-D (one dimensional) two-field model, inspired by the work of Bruch et al. 2014, is considered. This means that for any axial position, the model considers a fluid and a solid mean temperature. The energy conservation equations corresponding to the two fields read:

Fluid: $$\varepsilon \rho_f Cp_f \left[\frac{\partial T_f}{\partial t} + U \frac{\partial T_f}{\partial z}\right] = k_f \frac{\partial^2 T_f}{\partial z^2} + h_v(T_s - T_f) - H_{global}(T_f - T_{ext})$$

Solid: $$(1 - \varepsilon)\rho_s Cp_s \frac{\partial T_s}{\partial t} = k_s \frac{\partial^2 T_s}{\partial z^2} + h_v(T_f - T_s)$$

As can be seen from these equations, the two fields are thermally coupled through a convective heat transfer (h_v coefficient). In the fluid domain, we account for thermal losses (right-most term) and axial conduction (first term in the right-hand side). We also consider axial conduction for the solid field and accumulation terms for both fields. These can be derived from usual thermal-hydraulic equations assuming the following:

(i) The fluid velocity and the temperature evolutions are considered only in axial (i.e. vertical) direction, thus the governing equations are one-dimensional. This implies a transversal homogeneity of the oil and rocks temperatures.
(ii) The distributors are not included in the computational domain and conditions of uniform velocity

and temperature are considered at the inlet of the storage zone. This intends to represent a storage tank equipped with ideal distributors.
(iii) The rock bed is considered as a continuous, homogeneous and isotropic porous medium.
(iv) The properties of the rock bed are independent of temperature.

Some of the terms appearing in the two-field model are detailed below:

The axial thermal conduction between fluid layers:
$Q_{flowf} = A_{Tan} \times \lambda_{EqF}/h_{Seg} \times dT$

The axial thermal conduction in rocks:
$Q_{flowr} = \varepsilon_r \times A_{Tan} \times \lambda_{EqR}/h_{Seg} \times dT$

Convection between rocks and fluid is determined by the correlation of Wakao and Kaguei (1982):
$Nu=2+1.1xRe^{0.6}xPr^{1/3}$

Heat loss with ambient at 20°C:
$Q_{loss}=2 \times \pi \times k_{Ins} \times h_{Seg}/ln((r_{Tan} + d_{Ins})/r_{Tan}) \times dT$

The set of equation is then completed by a mass conservation equation and a simplified momentum equation assuming no head losses.

As for the pipe, these equations are then discretized using a finite volume method. This approach leads to a numerical model consisting of a series of axially distributed non-overlapping control volumes.

2.2.5 Numerical settings

The Dassl variable time step solver was used in the present work. To select the numerical settings, a convergence study was conducted for each parameter. For instance, the mesh size was progressively reduced up to the point where further refinement did not lead to significant result modification. This allows to identify a good compromise between computing resources and accuracy. The method was applied to the convergence criteria (i.e. a relative tolerance on the increments of the principal variables), the maximum allowed time-step during simulation and the axial mesh size in the solar field and the thermal storage. Finally, we used a 10^{-4} relative tolerance as the convergence criteria, a maximal time-step of 50 s and meshes of 5 m in length for the solar field and 6 cm in length for the thermal storage. These settings lead to computational duration of about a few min for a 12 h simulation.

3 Validation

3.1 Validation of the solar field model

In a first step, a calibration of the model was carried out for a specific day (Figure *4*). The objective was to determine the corrective coefficient (applied on the optical model output, see 2.2.2) in order to minimize the relative error between the model and experimental results. The model is fed with real DNI, solar position, inlet temperature and heat transfer fluid mass flow rate and it calculates the solar field outlet temperature that is compared to the experimental one. The relative error is given

by the ratio of the difference between theoretical and experimental powers to the theoretical power. The adjusted model is in the range of +/-10% of the experimental data except at the beginning and end of the day where the incertitude can be greater mainly due to limitations of the optical and thermal model for high incidence angles. The corrective coefficient especially includes soiling of the plant along with some model limitations but proves to be relatively constant according to our experience over successive days of operation.

In a following day, in order to validate the thermal-hydraulic modelling of the solar field, the prototype was operated to submit the solar field to an inlet temperature wave as shown in Figure *5*, while all other input variables remain unchanged. Again, the model is fed with real DNI, solar position, inlet temperature and heat transfer fluid mass flow rate. This allows to check the dynamic behavior of the solar field by comparing the simulated outputs and the experimental ones. At time t=1950 s, the inlet temperature of the solar field decreases from 160°C to 135°C (amplitude of 25°C) in 100 s and then returns back to nominal temperature after 150 s (total duration 250 s). Due to experimental limitations, it was not possible to get a sharper signal. In the calculation, the inlet temperature of the solar field is imposed equal to the experimental one as can be seen in Figure *5*. After 6 min (360s), the outlet temperature of the solar field shows a similar behavior both in the model and experimentally. A wave with an amplitude of about 10°C and 450 s duration is observed: the amplitude is reduced compared to the inlet signal and the duration is longer. This is due to the system's inertia and the simulation reproduces correctly this dynamic behavior. The global increase of temperature between entrance and exit of the solar field is due to solar power input.

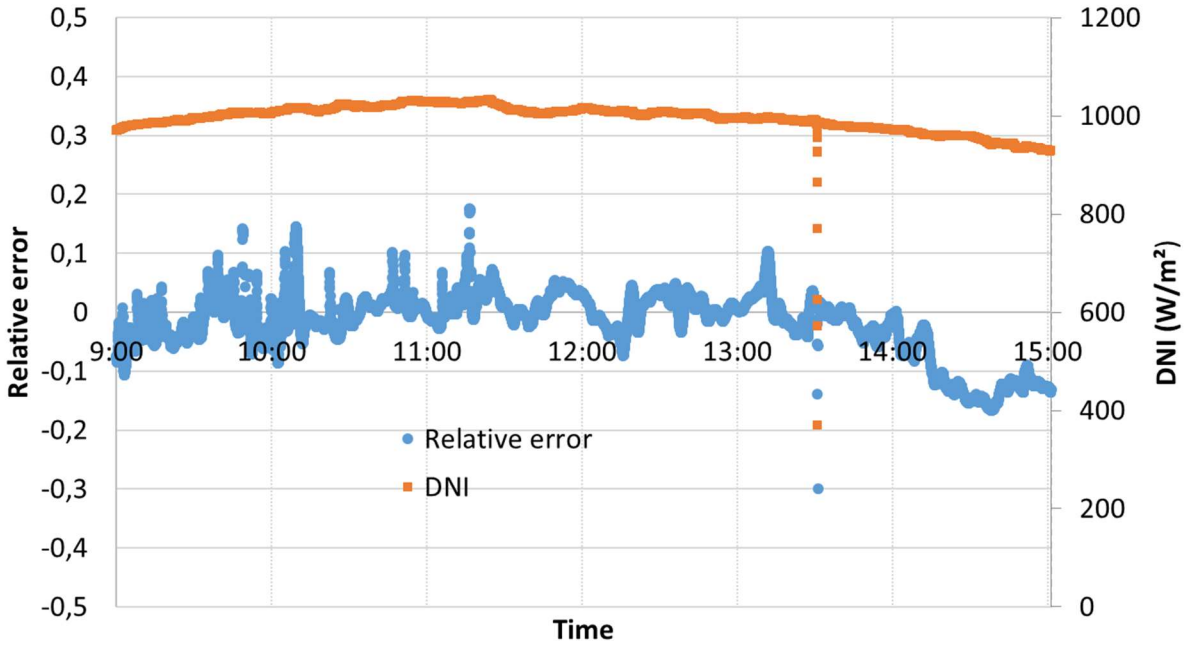

Figure 4 : Relative error between the numerical and experimental data over a day (prototype thermal power output) along with DNI

In order to illustrate this phenomena, the same case is simulated while neglecting the thermal capacity of the pipe. In practice, the specific heat capacity of the metal is divided by 100 in the model. The results are shown on the "no inertia" curve in Figure *5*. It can be observed that in this case, the output

signal is not different from the input temperature wave. The temperature wave exits the solar field earlier (3 min fluid travel time instead of 6 min when thermal inertia in considered). In fact, 3 min correspond simply to the residence time of the fluid (ratio between piping volume and volumetric flow-rate). Since maintaining the output temperature to a set-point value is the main control challenge of a solar power plant, thermal inertia has to be properly taken into account in order to manage signal delay. These results validate the solar field parametrization.

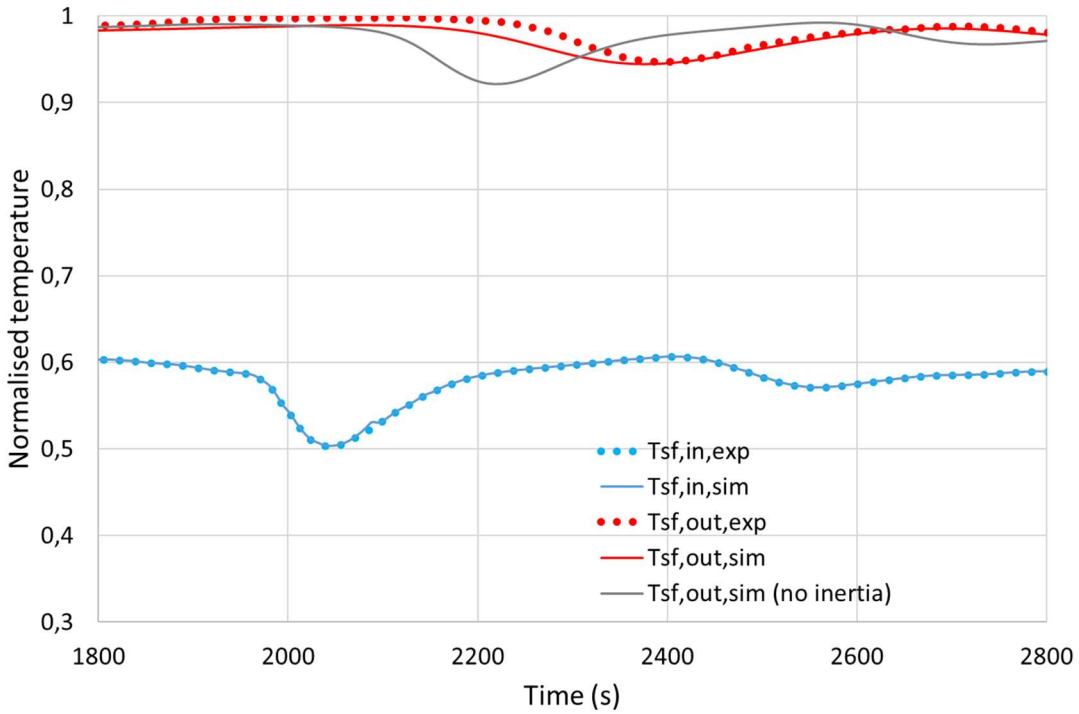

Figure 5 : Impulse on the inlet temperature of the solar field and exit temperature (simulation (sim) vs. experiment (exp))

In Figure *6*, pressure losses during the same run as in Figure *5* are compared to the experimental ones. Good quantitative and qualitative results are obtained before 1800s, then even if the global trend is correct, a higher error is observed during the temperature wave transient. This could be further explored to improve the model but is of limited importance as far as the prototype operation is concerned. Note that the time scale is larger than in Figure *5* in order to show the influence of previous flowrate variations on the pressure drop before 1800 s. Pressure losses oscillate around 0.23 bar for each solar field. Only linear pressure losses are represented but they are dominating over singular ones. Mass flowrate measured at the pump exit is also plotted and it shows small variations that directly impact pressure drop. At time t=1200 s and t=1800 s, flowrate increases and it is visible both on the experimental and simulated pressure drops. At time t=2000 s, when the cold temperature wave enters the solar field, pressure loss increases in SF1 (both for experimental and simulation results). This is due to the increase of the oil viscosity at lower temperature. At the same time, there is a small decrease of the pressure loss in SF2 due to fluid contraction in SF1 that reduces temporarily the

flowrate in SF2 (obtained by simulation). This fluid contraction is linked to higher density of cold oil that is fed around t=2000 s in SF1. Eventually, the pressure losses are well estimated and can provide reliable information for operation and design purposes. Moreover small transients such as fluid contraction can be tracked even though its impact is low for this kind of heat transfer fluid.

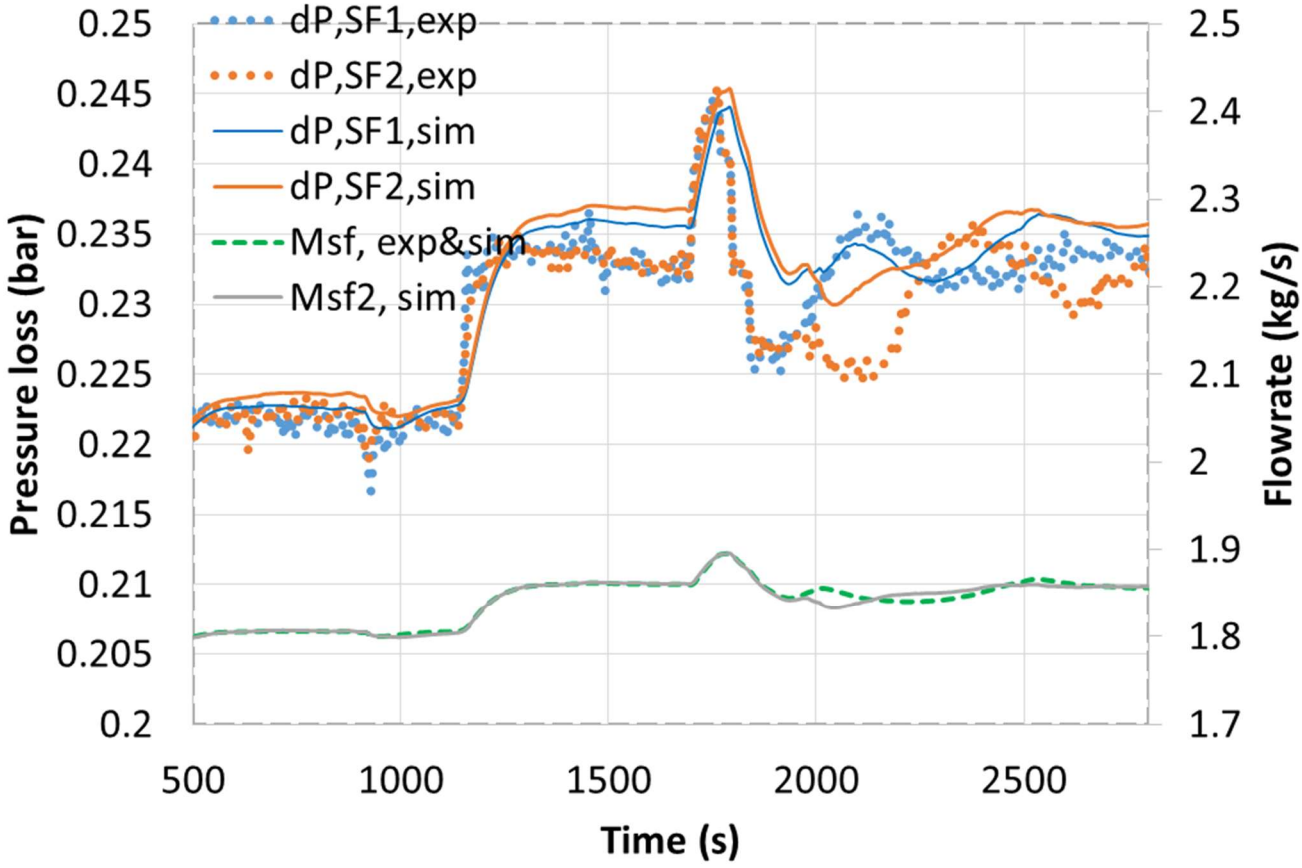

Figure 6 : Pressure loss on both solar fields (simulation (sim) vs experiment (exp)) along with flowrate (at the pump and at the entrance of SF2)

3.2 Validation of the storage model

The storage model was previously validated against (Pacheco et al, 2002) in (Bruch et al., 2014) but it is of interest to compare it against new experimental results obtained with our thermocline thermal storage using oil instead of sodium and potassium nitrate. A charge and discharge cycle was applied on the storage tank. It was charged at T_{Charge} and discharged at $T_{Discharge}$ with T_{Charge}-$T_{Discharge}$=150°C. Prototype-scale thermal energy storage (TES) systems are less instrumented than lab-scale TES tanks as they are more devoted to in-site and in-process proof of concept than fine and local experimental characterization. As a consequence, initial axial temperature profile may not be precisely known, which may lead to significant differences after hours of process. In this case, performing middle-term simulations (weeks instead of single tests) compensates lack of embedded instrumentation and allow to significantly enhance the numerical/experimental agreement (Bruch et al., 2017b). Consequently, the initial temperature given in Figure *7* corresponds to the result of a middle-term simulation. Charge was stopped when the exit temperature reached T_{Charge}-90°C and discharge was stopped when exit temperature of the storage reached $T_{Discharge}$+90°C. Nominal flowrate is 1.4 kg/s.

The results are presented using dimensionless variables defined as in (Bruch et al. 2017a):

$$T^* = \frac{(T_f - T_{Discharge})}{(T_{Charge} - T_{Discharge})} \qquad \text{Equation 1}$$

$$z^* = \frac{z}{h_{tank}} \qquad \text{Equation 2}$$

$$m^* = \frac{\dot{m}}{\dot{m}_{nom}} \qquad \text{Equation 3}$$

As displayed in Figure 7, the simulated temperature profile and the measured temperatures show good agreement both at the end of the charge and at the end of the discharge. The area between the two curves enables to evaluate the stored energy. The thermocline zone is clear and occupies about 1/5 of the storage height. This low value is due to the fact that important part of the thermal gradient is pushed out the storage tank during charge and discharge modes. This kind of operating control is relevant with effective CSP power plant thermal storage operating control and allows to reach high storage capacity.

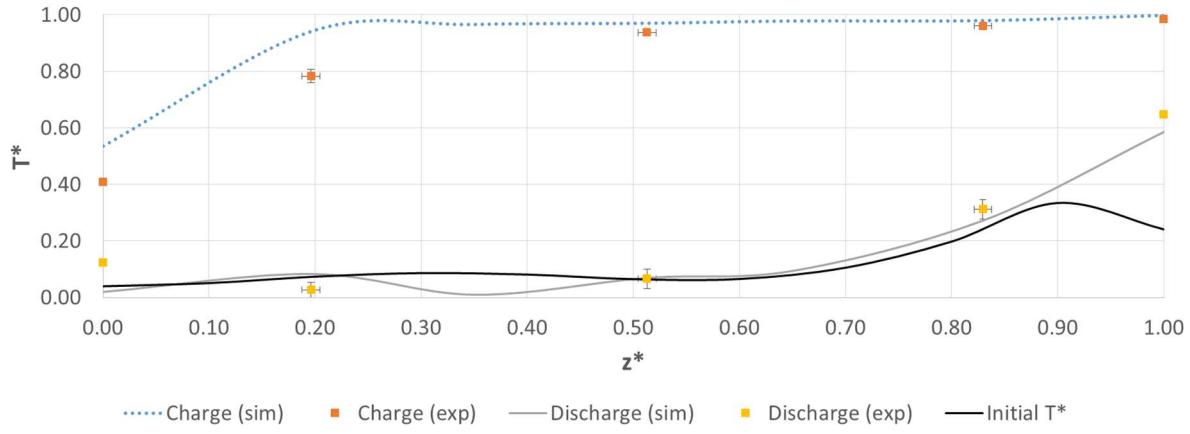

Figure 7: Temperature profile in the storage at the end of charge and end of discharge process (lines represent simulated results, dots indicate measured values)

Small differences between experiments and simulations are mainly attributable to initialization of the storage temperature since only three storage levels are instrumented. Since the storage has a pilot scale, it has been weakly instrumented to minimize fabrication costs and to ensure reliability. Consequently, temperature measurements have been optimized to provide sufficient information especially for operation.

Another way to validate the model is to check output temperatures during charging and discharging processes. In Figure *8*, the dimensionless exit temperatures of the storage during charge and discharge are displayed for simulated and experimental values. A good agreement is obtained all along the run

both for charging and discharging processes. It shows that even with limited instrumentation on the storage tank, it is possible to predict its behavior with accuracy.

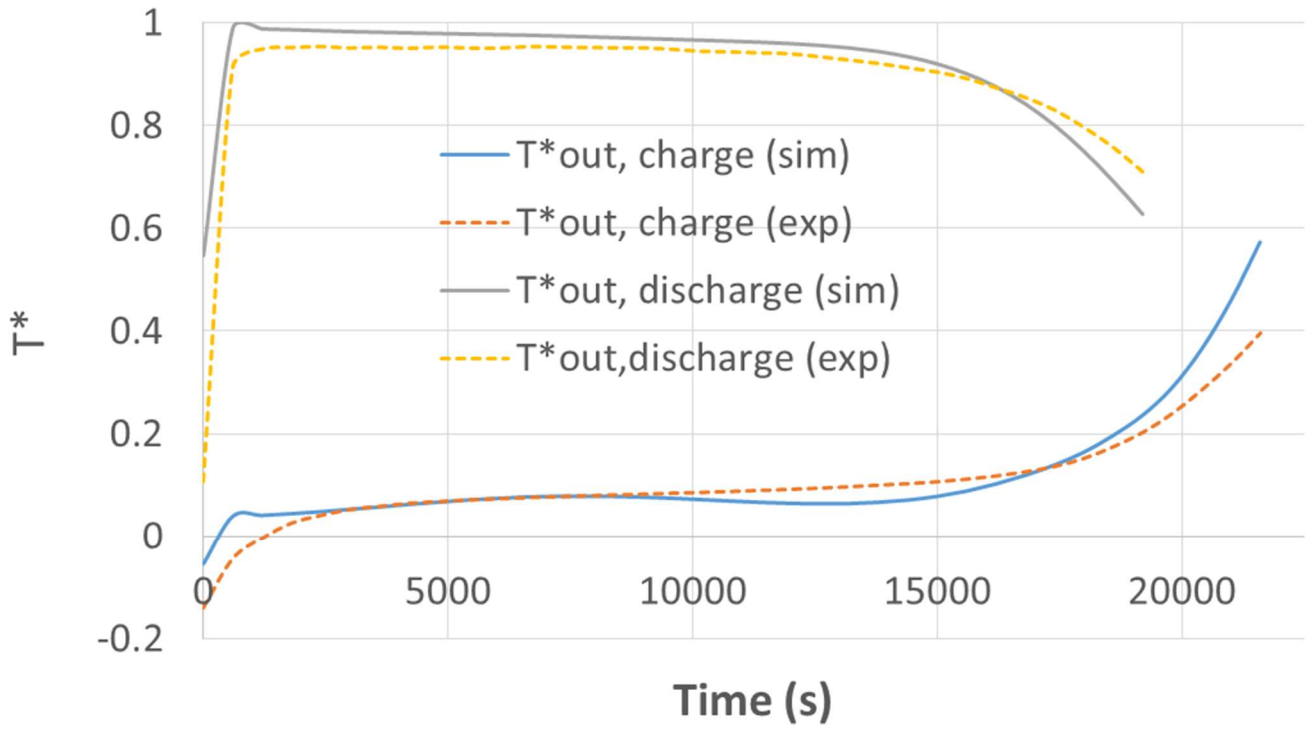

Figure 8: Temperature profiles at storage outlet during charge and discharge (lines represent simulated results, dashed lines indicate measured values)

4 Dynamic analysis of the whole solar thermal prototype

All the previously validated components are integrated in a global model of the installation that is composed of the solar field, the thermal storage and a heat sink to mimic the ORC module as schematized in Figure *9*. The model also includes controllers for the solar field flowrate and for the focalization of mirrors. The whole model represents a set of more than 2 thousands equations. The developed dynamic model permits to highlight specific dynamic behaviors. Three specific configurations will be exposed in the following part. Startup procedure can be tricky. The storage operation has also to be investigated with the best use of the thermocline zone. Moreover, the solar field outlet temperature regulation remains a major concern.

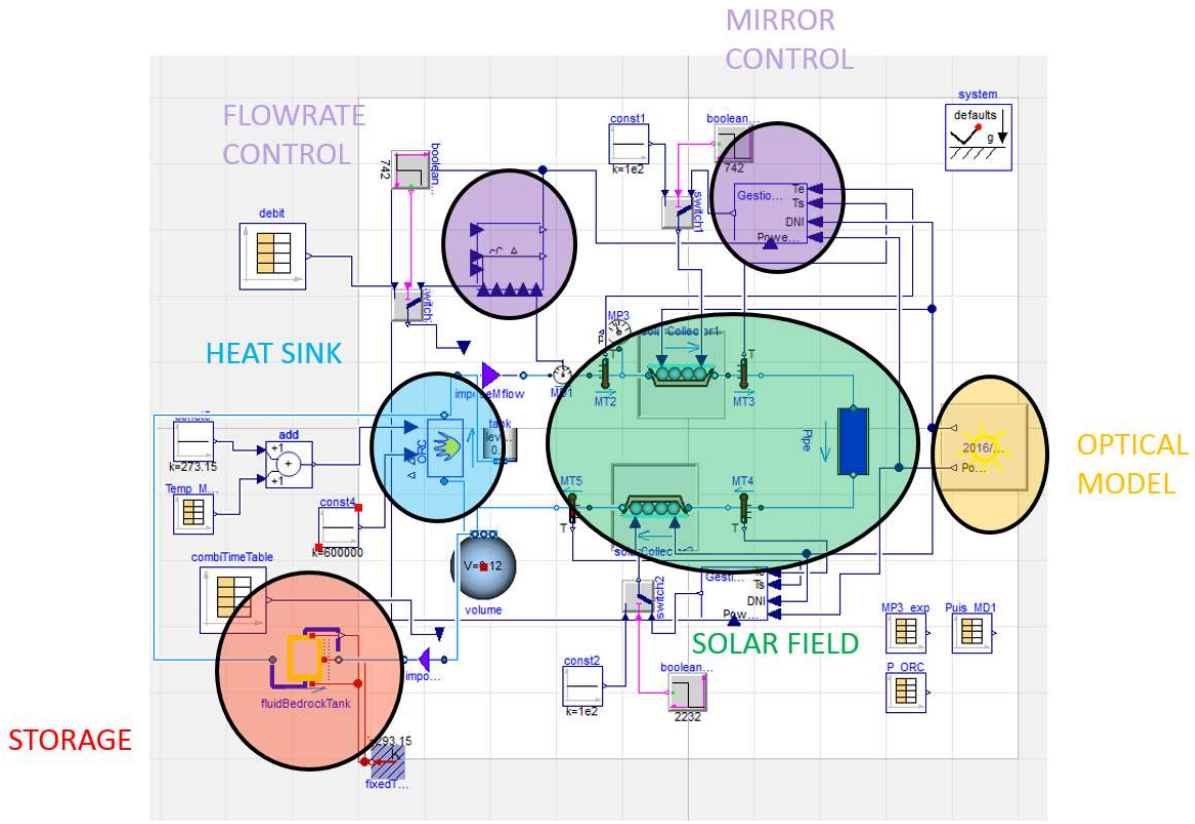

Figure 9: Global model of the prototype on the DYMOLA simulation platform

4.1 Startup procedure

During startup operation or commissioning of storage, cold oil (i.e. 20°C or below) is fed into the solar field. Due to high viscosity of oil at such a low temperature, pressure losses may be high leading to low flowrate and laminar flows. Consequently, due to poor heat transfer coefficient, if all mirrors are focalized, overheating of pipe walls may occur depending on the incident heat flux. A maximum inside wall temperature of 350°C is considered in order to prevent the selective coating damage and increase thermal oil durability. This limit can be exceeded as illustrated by the model in Figure *10* during startup phase for a 20 kW/m² heat flux at the receiver when all mirrors are focalized. Indeed it shows a pipe wall peak temperature of 362°C at time t=550s. Note that pipes are 55 m in length for each solar field, they are spatially discretized in 10 segments, which means that this temperature is a mean value over 5.5 m. After this peak, a decrease in wall temperature is observed because of an increase in Reynolds number linked to an increase in oil temperature that lowers the viscosity. In order to respect the operating limits, it is recommended to defocalize some mirrors in order to maintain pipe wall temperature within an acceptable range. Indeed, by limiting the power input by 60% during the first 10 min of startup procedure, it enables to maintain the pipe wall temperature below 350°C as shown in Fig. 9. Thus dynamic control permits to optimize durability of both oil and selective coating while maximizing focalization.

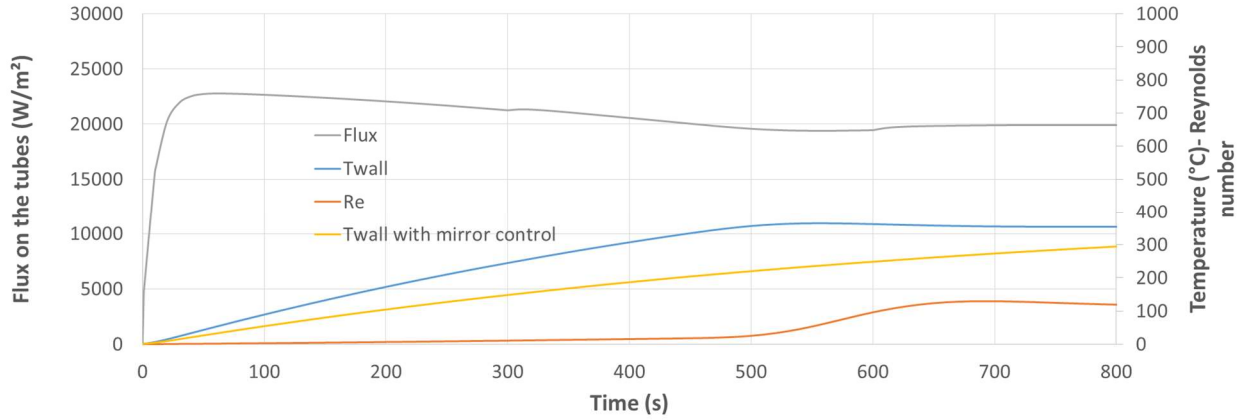

Figure 10: Heat flux on the pipes, Reynolds number and wall temperature at the entrance of the solar field (cold start)

4.2 Storage mode

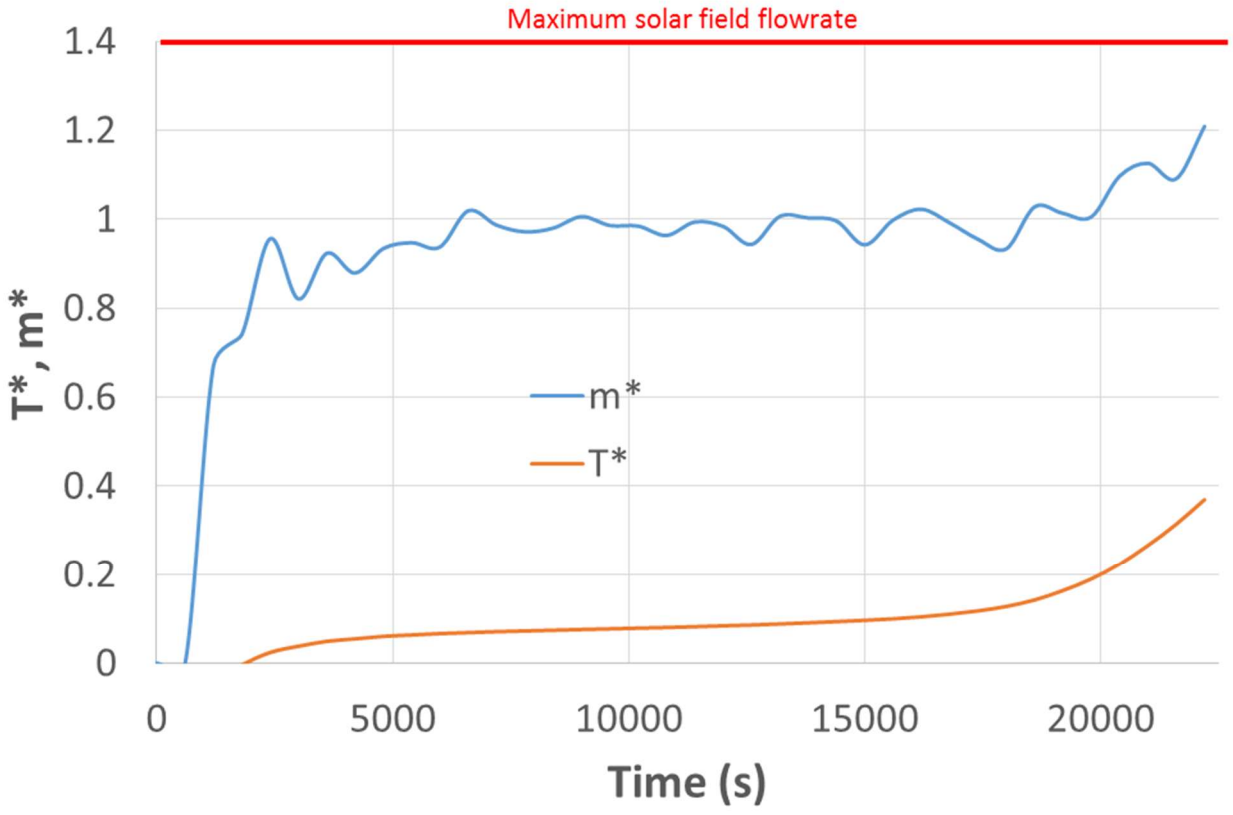

Figure 11: Dimensionless storage flowrate and temperature at storage outlet (experimental)

Figure *11* shows the normalized flowrate (Equation *1*) during the charging process already presented in Figure *8*. During this test, the total flowrate in the solar field is directed toward the thermal storage. Consequently the storage flowrate and the solar field flowrate are identical (Msto=Msf). Dimensionless temperature at storage outlet is also plotted. At the end of the storage process, the outlet temperature

of storage increases because the thermocline is pushed out of the storage. This results in a drastic temperature increase for the inlet temperature of the solar field which implies an increase of the flowrate in order to maintain a constant solar field temperature outlet (see section 4.3). In Figure *11* a 20% increase of the nominal flowrate is observed but it could be much higher depending on the outlet temperature of the storage and power available on the solar field. A +40 % margin on the nominal flowrate is accepted as an upper limit, in case this value is exceeded, then defocalisation of some mirrors will be necessary to maintain a constant solar field output temperature.

On the one hand, it appears that pushing out the thermocline at the end of the charging process can be critical for the flowrate required in the solar field (high flow rate means high pressure loss). On the other hand, pushing out the thermocline is favorable to maximize the storage capacity of the tank. Consequently, dynamic simulation of the whole solar power plant is required to optimize the control strategy. It enables to guaranty the best utilization of the storage (pushing out of the thermocline) while ensuring proper operation within the solar field limits (maximum flowrate) along with maximum utilization of incident power (minimum defocalisation).

4.3 Temperature regulation

Solar field outlet temperature control is of main importance in solar power plants due to temperature constraints imposed by turbines. Various control schemes can be evaluated thanks to dynamic modeling. As an example we propose to evaluate the response a simple PID regulator and a PID+feedforward regulator as described in Figure *12*Figure *11* (Rodat et al., 2015). Feedforward consists in a simple static thermal model of the plant described in details in (Rodat et al., 2016) that provides a guess value of the flowrate to the PID regulator so that its response is faster. Figure *12* displays the solar field outlet temperature for the two control schemes (PID and PID+feedforward) along with the DNI. Temperature is normalized by the maximum temperature. After a stabilization period, at t=9100 s, a DNI step from 900 W/m² to 400 W/m² is imposed to the solar field model along with a second step at t=12700 s from 400 W/m² back to 900W/m². PID parameters are kept the same between the two schemes so that the influence of feedforward only is illustrated. It can be observed that the temperature goes below set point when the DNI decreases whereas overshoot of the set point occurs when DNI is increasing. With a simple PID, the solar field outlet temperature is +/- 12% (+/- 40°C) of the set point while introducing feedforward limits the solar field temperature in the range of +/- 3% (+/- 10°C) of the set point. Temperature overshoots can be especially critical for the heat transfer fluid lifetime. They could be even more smoothed by introducing DNI short-term previsions in the controller for anticipation.

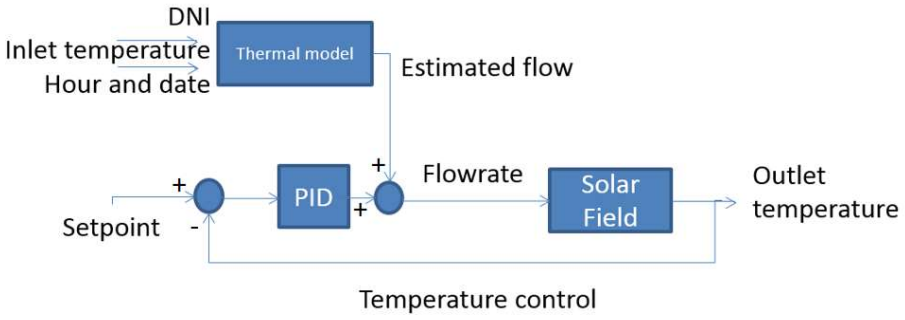

Figure 12: Scheme of the solar field outlet temperature control loop including PID+feedforward

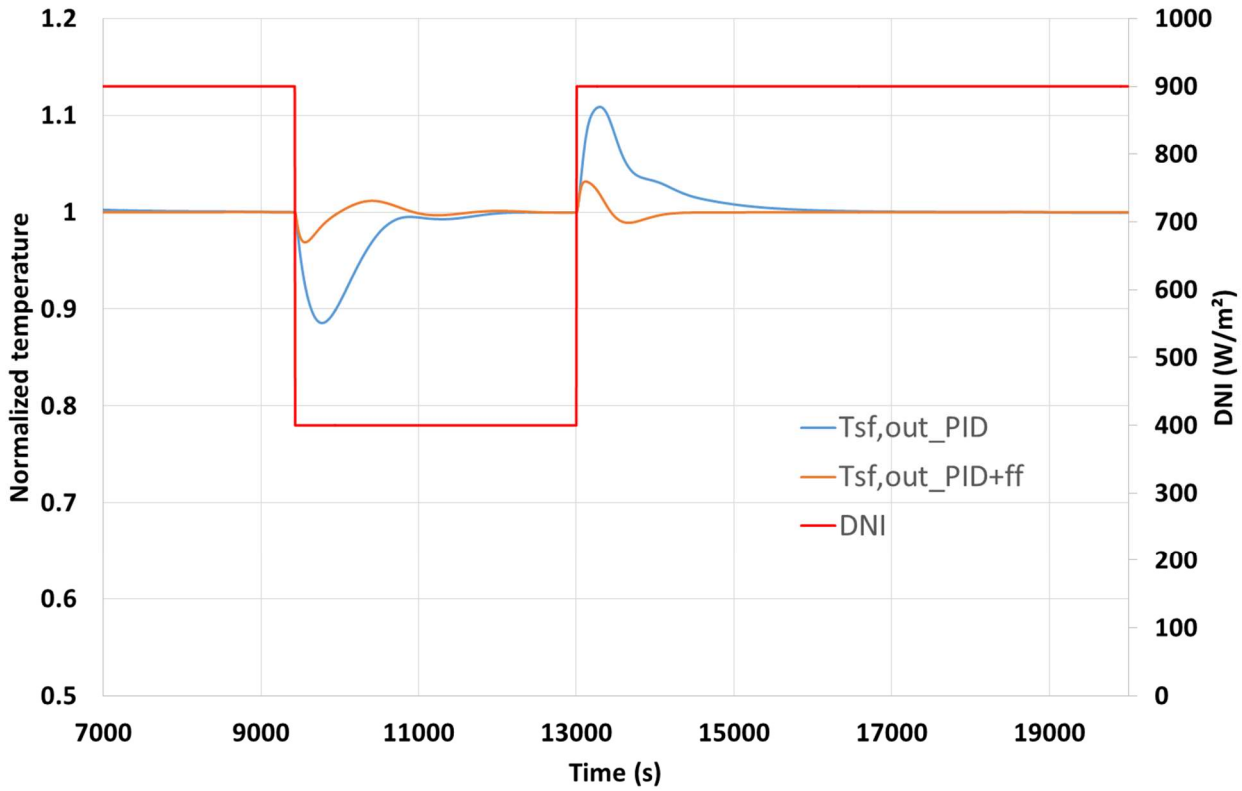

Figure 13: DNI and normalized outlet temperature of the solar field for two control schemes: PID and PID plus feedforward.

5 Conclusion

A multi-domain dynamic simulator of a concentrated solar plant is established. It consists of a Fresnel solar field coupled with a thermocline thermal storage, an organic Rankine cycle and the associated control. The model takes the form of a single large-scale Modelica problem. The heat transfer fluid is oil both in the solar field and storage. The numerical results are validated against experimental data obtained on the corresponding prototype.

The optical and thermal model proposed is simple (8 temperature nodes, 2 bands) but is able to estimate the plant thermal efficiency with a relative error below 10%. The uncertainty of the model can especially be linked to the optical model simplification (10° resolution of the optical efficiency matrix, homogenous flux on the receiver, impact of soiling…). It could be improved by using direct raytracing results instead of a simplified optical efficiency matrix.

Classical thermo-hydraulic models (1D, monophasic) are able to fairly describe the transport of a temperature wave in the solar field and thus are adapted to investigate temperature control of a solar plant. Interesting results were obtained for pressure losses even if local discrepancies can be highlighted. They were not further investigated due to low impact on the plant operation and control.

The storage model provides good agreement with the analyzed data. Future work will include partial cycling behavior of the thermocline.

Finally, at the solar plant level, the model was able to highlight possible critical situations and provides capabilities for exploring optimal control solutions. It is thus a valuable tool for operation, sizing of future installations and risk analysis.

Acknowledgements:

The authors gratefully acknowledge ALSOLEN-TECH Company for its financial support for the Alsolen-mid demonstrator and associated experimental and numerical studies.

Nomenclature

A_{Tan}: Tank section (m²)

d_{Ins}: Insulation thickness (m)

D: Internal diameter of the pipe (m)

dPSF1: Pressure loss in the first solar field (bar)

dPSF2: Pressure loss in the second solar field (bar)

e : Window thickness (m)

e_l : Spectral emissive power distribution (W/m²/µm)

h: Convective heat transfer coefficient (W/m²/K)

h_{Seg}: Height of a storage discretization layer (m)

I_i : Thermal inertia in volume control i per surface unit (J/K/m²)

k_{Ins}: Thermal conductivity of insulation (0.2 W/m/K)

L: Length of the pipe (m)

$\dot{m}$: Heat transfer fluid flow rate (kg/s)

$\dot{m}_{nom}$: Nominal heat transfer fluid flow rate (kg/s)

Msto: Mass flow-rate in the storage tank (positive in charging mode) (kg/s)

Msf: Mass flow-rate in the solar field pump (kg/s)

Msf2: Mass flow-rate in the solar field 2 (kg/s)

Nu: Nusselt number (-) defined as $\frac{h.D}{\lambda}$

Nu_{lam}: Nusselt number for laminar flow (-)

Nu_{turb}: Nusselt number for turbulent flow (-)

Nu_{trans}: Nusselt number for laminar-turbulent transition flow (-)

Pr: Prandtl number (-)

$\dot{Q}^{i\to j}$: Convective flux from i to j (W/m²)

$\dot{Q}_{cond}^{i\to j}$: Conductive flux from i to j (W/m²)

Re: Reynolds number (-) defined as $\frac{\rho.U.D}{\mu}$

r_{Tan}: Tank radius (m)

SF1: First solar field

SF2: Second solar field

T_{Charge}: Fluid temperature during storage charge (°C)

$T_{Discharge}$: Fluid temperature during storage charge (°C)

T_f : Fluid temperature (°C)

T*: Dimensionless temperature

Tsf,in: Temperature at inlet of the solar field (°C)

Tsf,out: Temperature at outlet of the solar field (°C)

Tsto,uf: Temperature at the upper flange of the storage (°C)

Tsto,lf: Temperature at the lower flange of the storage (°C)

Tsto,top: Temperature at the top zone of the storage (°C)

Tsto,medium: Temperature at the medium zone of the storage (°C)

Tsto,bottom: Temperature at the bottom zone of the storage (°C)

U: Fluid mean velocity in pipe (m/s)

z : Altitude of the considered storage section (0 at the bottom) (m)

z*: Dimensionless altitude

ε_r: Rock volume fraction (-)

λ: Thermal conductivity (W/m/K)

λ_{EqF}: Equivalent vertical thermal conductivity in fluid (0.5 W/m/K)

λ_{EqR}: Equivalent vertical thermal conductivity in rock (5 W/m/K)

f_{lam}: Darcy coefficient for laminar flow (-)

f_{turb}: Darcy coefficient for turbulent flow (-)

f_{trans}: Darcy coefficient for laminar-turbulent transition flow (-)

ϕ_i^I : Incident flux in control volume i (W/m²)

ϕ_i^r : Reflected flux in control volume i (W/m²)

ϕ_i^{α} : Absorbed flux in control volume i (W/m²)

ϕ_i^{τ} : Transmitted flux through control volume i (W/m²)

ϕ_i^{e} : Emitted flux in control volume i (W/m²)

ρ: Fluid density (kg/m^3)

μ: Dynamic viscosity (Pa.s)

References

Al-Maliki W.A.K., Alobaid F., Kez V., Epple B., Modelling and dynamic simulation of a parabolic trough power plant, Journal of Process Control, 39, 2016a, 123-138.

Al-Maliki, W. A. K., Alobaid, F., Starkloff, R., Kez, V., & Epple, B. (2016). Investigation on the dynamic behaviour of a parabolic trough power plant during strongly cloudy days. *Applied Thermal Engineering*, *99*, 2016b, 114-132.

Aurousseau A., Vuillerme V., Bezian J.J., Control systems for direct steam generation in linear concentrating solar power plants–A review.*Renewable and Sustainable Energy Reviews*, *56*, 2016, 611-630.

Biencinto M., Bayon R., Rojas E., Gonzalez L., Simulation and assessment of operation strategies for solar thermal power plants with a thermocline storage tank, Solar Energy, 103, 2014, 456-472.

Birnbaum J., Feldhoff J.F., Fichtner M., Hirsch T., Jöcker M., Pitz-Paal R., Zimmermann G., Steam temperature stability in a direct steam generation solar power plant, Solar Energy, 85, 2011, 660-668.

Bruch, A., Fourmigué, J. F., & Couturier, R. Experimental and numerical investigation of a pilot-scale thermal oil packed bed thermal storage system for CSP power plant. *Solar Energy*, *105*, 2014, 116-125.

Bruch, A., Molina, S., Esence, T., Fourmigué, J. F., & Couturier, R. (2017a). Experimental investigation of cycling behaviour of pilot-scale thermal oil packed-bed thermal storage system. *Renewable Energy*, *103*, 277-285.

Bruch, A., Experimental Characterization of a Prototype-Scale Dual-Media Thermocline TES and Ways to Enhance its Numerical Simulation, Solarpaces 2017b, Santiago (Chile).

Carvill J., Mechanical engineer's data handbook, 1993, ISBN 9781483193731.

Cocco D, Serra F, 2015. Performance comparison of two-tank direct and thermocline thermal energy storage systems for 1 MWe class concentrating solar power plants. Energy 81: 526-536.

DLR, 2001. Greenius Energy Yield Calculation Software.

Eck M., Hirsch T., Dynamics and control of parabolic trough collector with direct steam generation, Solar Energy, 81, 2007, 268-279.

Esence, T., Bruch, A., Molina, S., Stutz, B., & Fourmigué, J. F. (2017). A review on experience feedback and numerical modeling of packed-bed thermal energy storage systems. *Solar Energy*, *153*, 628-654.

Garcia I.L., Alvarez J.L., Blanco D., Performance model for parabolic trough solar thermal power plants with thermal storage: Comparison to operating plant data, Solar Energy, 85, 2011, 2443-2460.

Giraud, L., Bavière, R., Vallée, M., & Paulus, C. (2015, September). Presentation, Validation and Application of the DistrictHeating Modelica Library. In Proceedings of the 11th International Modelica

Conference, Versailles, France, September 21-23, 2015 (No. 118, pp. 79-88). Linköping University Electronic Press.

Gnielinsky V., New equation for heat and mass transfer in turbulent pipe and chanel flow . Int. Chem. Eng., 16, 1976.

Ju, X., Xu, C., Wei, G., Du, X., & Yang, Y. (2016). A novel hybrid storage system integrating a packed-bed thermocline tank and a two-tank storage system for concentrating solar power (CSP) plants. *Applied Thermal Engineering*, *92*, 24-31.

Manenti F., Ravaghi-Ardebili Z., Dynamic simulation of concentrating solar power plant and two-tanks direct thermal energy storage, Energy, 55, 2013, 89-97.

Manzolini G., Giostri A., Saccilotto C., Silva P., Macchi E., Development of an innovative code for the design of thermodynamic solar power plants part A: Code description and test case, Renewable Energy, 36, 2011a, 1993-2003.

Manzolini G., Giostri A., Saccilotto C., Silva P., Macchi E., Development of an innovative code for the design of thermodynamic solar power plants part B: Performance assessment of commercial and innovative technologies, Renewable Energy, 36(9), 2011b, 2465-2473.

Morin G., Dersch J., Eck M., Häberle A., Platzer W., Comparison of linear Fresnel and parabolic trough collector systems - influence of linear Fresnel collector design variations on break even cost, Solarpaces 2009, Berlin (Germany).

NREL, 2014. System Advisor Model Version 2014.1.14 (SAM 2014.1.14) [Web page]. National Renewable Energy Laboratory.

Olsson H. et al., 2014, Modelica® - A Unified Object-Oriented Language for Systems Modeling Language Specification Version 3.3 Revision 1, available at https://www.modelica.org/documents/ModelicaSpec33Revision1.pdf

Pacheco J.E., Showalter S.K., Kolb W.J., Development of a molten-salt thermocline thermal storage system for parabolic trough plants. *Journal of solar energy engineering*, *124*(2), 2002, 153-159.

Powell K.M., Edgar T.F., Modeling and control of a solar themal power plant with thermal energy storage, Chemical Engineering Science, 71, 2012, 138-145.

Reddy V.S., Kaushik S.C., Ranjan K.R., Tyagi S.K., State-of-the-art of solar thermal power plants—A review. *Renewable and Sustainable Energy Reviews*, *27*, 2013, 258-273.

Rodat S., Tantolin C., Le Pivert X., Lespinats S., Daily forecast of solar thermal energy production for heat storage management, Journal of Cleaner Production, 139, 2016, 86-98.

Rodat S., Bruch A., Dupassieux N., El Mourchid N., Unique Fresnel demonstrator including ORC and thermocline direct thermal storage: operating experience, Energy Procedia, 69, 2015, 1667-1675.

Rodat S., Souza J.V.D., Thebault S., Vuillerme V., Dupassieux N., Dynamic simulations of Fresnel solar power plants, Energy Procedia, 49, 2014, 1501-1510.

Soares, J., & Oliveira, A. C. (2017). Numerical simulation of a hybrid concentrated solar power/biomass mini power plant. *Applied Thermal Engineering*, *111*, 1378-1386.

Stark C., Pless J., Logan J., Zhou E., Arent D.J., Renewable Electricity: Insights for the Coming Decade, NREL/TP-6A50-63604, 2015.

Stuetzle T., Blair N., Mitchell J.W., Beckman W.A., Automatic control of a 30 MWe SEGS VI parabolic trough plant, Solar Energy, 76, 2004, 187-193.

Valenzuela L., Zarza E., Berenguel M., Camacho E.F., Control concepts for direct steam generation in parabolic troughs, Solar Energy, 78, 2005, 301-311.

Vidal, F., Chandez, B., & Albert, R. (2017, June). Development of an alternative low-cost solar collector working at medium temperature (150–250° C). In *AIP Conference Proceedings* (Vol. 1850, No. 1, p. 020016). AIP Publishing.

Wakao, N. & Kaguei, S., Heat and Mass Transfer in Packed Beds. Gordon and Breach Science Publishers, New York, 1982.

Zigrand D.J., Sylvester N.D. , Turbulent-flow friction-factor equations, Chemical engineering, 29, 1965, 86-87.